DOI 10.1007/s11029-019-09789-x
Mechanics of Composite Materials, Vol. 55, No. 1, March, 2019 (Russian Original Vol. 55, No. 1, January-February, 2019)

NUMERICAL MODELING OF THE CASTING PROCESS AND IMPACT LOADING OF A STEEL-FIBER-REINFORCED HIGH-PERFORMANCE SELF-COMPACTING CONCRETE

J. Sliseris* **and A. Korjakins**

Keywords: *fiber-reinforced concrete, local fiber orientation, two-phase flow, impact modeling*

With the rapid development of high-performance self-compacting fiber-reinforced concrete materials, advanced numerical modeling tools have become necessary to design optimum materials and structures. A simulation framework that includes numerical modeling of the flow of a high-performance self-compacting fiber-reinforced concrete mortar during the casting process, calculation of local fiber orientation based on the deformation gradient in the mortar, and impact modeling taking into account the local fiber orientation is proposed. A new method to calculate the probability of fiber orientation distribution by particle tracking and approximation of particle motion using the deformation gradient is proposed. A discrete lattice modeling technique, with a nonlinear strain-rate- and local-fiber-orientation-dependent constitutive law for a numerical impact modeling is proposed. Single- and three-point concrete casting techniques are numerically simulated, and results are compared with experimental measurements, showing a good agreement. The numerical models revealed that fiber orientation and the impact resistance of beams strongly depended on the casting technology of the self-compacting concrete. The numerical model proposed can be used to design efficient concrete casting technologies ensuring the necessary fiber orientation in load-bearing structures..

1. Introduction

High-performance fiber-reinforced concrete (HPFRC) and ultrahigh-performance fiber-reinforced concrete (UHPFRC) are becoming more and more popular in the society of civil engineers. However, the influence of casting technology on the fiber orientation and fracture mechanics of HPFRC and UHPFRC have not been well understood yet, especially when a self-compacting fiber-reinforced concrete is used. Fiber orientation plays a great role due to the bridging effect of fibers in cracks of beams, frames, and plates.

Faculty of Civil Engineering, Riga Technical University, Riga, Latvia
*Corresponding author; e-mail: janis.sliseris@gmail.com

Russian translation published in Mekhanika Kompozitnykh Materialov, Vol. 55, No. 1, pp. 43-60, January-February, 2019. Original article submitted May 2, 2018.

One possibility of orienting fibers is to take advantage of the fact that they tend to be aligned perpendicular to the flow of self-compacting concrete. This effect, with a special pouring technique, is used to manufacture HPFRCs with oriented fibers [1-3]. Another way to achieve the necessary fiber orientation is to use the gradient of flow speed and local effects near formwork surfaces [4-7]. Accurate numerical models could help one to better understand the influence of casting technology on the mechanical behavior of load-bearing structures.

The casting process of concrete can be modeled numerically using either continuum-based or discrete-element methods, e.g., the Lagrangian smooth particle hydrodynamics (SPH) [8]. A continuum-based method that estimates the probability distribution function of fiber orientation is described in [9]. However, there is proposed only a 2D method, without a clear description of how to establish a link between it and solvers for structural mechanics. In SPH, the fluid is replaced by discrete particles without a direct link to the actual internal structure of mortar. Moreover, there are not enough information on the influence of smoothing parameters on simulation results. Most of the validated codes of computational fluid dynamics (CFD) use solvers based on Navier–Stokes equations,and this approach is also used in that research.

Virtual computer models of structural elements could help one to understand and design new materials and structures. Currently, numerical models for dynamically and statically loaded pure [10] and fiber-reinforced concrete [11-14] that are based on the continuum theory are available. But the micro- and mesostructures of the concrete are difficult to represent as a continuum because of the large number of different-size aggregates, voids, and other heterogeneities present in it [10,11,15]. Due to the heterogeneity of concrete, the load is transferred by discrete load paths. The discrete nature of concrete has promoted the development of discrete-element models (DEM) with triangular, tetrahedral, hexahedral, or another type of lattices [16-18].

Owing to the complex material behavior of self-compacting fiber-reinforced concrete, an accurate constitutive model is necessary to achieve a reasonable accuracy by numerical methods. A thermodynamically consistent cohesive model for the DEM of cement-based materials is presented in [19]. The propagation of cracks in concrete is studied in [19] using a cubic distinct lattice spring model [20]. A fracture analysis of reinforced concrete structures is performed in [21] employing a micropolar peridynamic analysis framework [21]. The mechanical behavior of ultrahigh-performance concrete (UHPC) is successfully approximated in [22] for projectile penetration impact loads by using a discrete lattice particle model [22]. The optimum material orientation as the key factor in designing composite structures is introduced in [23]. Later, this elastic-energy-based approach was extended to the analysis of 2D linear and nonlinear elastic materials [24-26] and 3D linear elastic materials [27-29]. However, the effect of local, nonuniform fiber orientation was not taken into account.

So far, there is no information on a numerical modeling technique that can explicitly capture the influence of casting technology on the impact properties of a self-compacting high-performance fiber-reinforced concrete. In our work, a new method for postprocessing the simulation results of two-phase flow of mortar and for calculating the probability of fiber orientation distribution that can be used directly in a constitutive model is proposed. Moreover, a constitutive model that can capture the effect of local fiber orientation and strain rate is also advanced.

2. Numerical Models

2.1. Fiber orientation analysis using CFD results

The casting process of an incompressible two-phase mortar was modeled using the CFD finite-volume solver. The momentum, continuity, and transport equations for the volume fraction of fluid are [30–32]

$$\frac{\partial \rho U}{\partial t} + \nabla(\rho UU) - \nabla\rho\nabla U - \rho g = \nabla p - F_s ,$$

$$\nabla \cdot U = 0 ,$$

$$\frac{\partial Y}{\partial t} + \nabla\left[(\gamma U) + \nabla\gamma(1-\gamma)U_r\right] = 0 ,$$

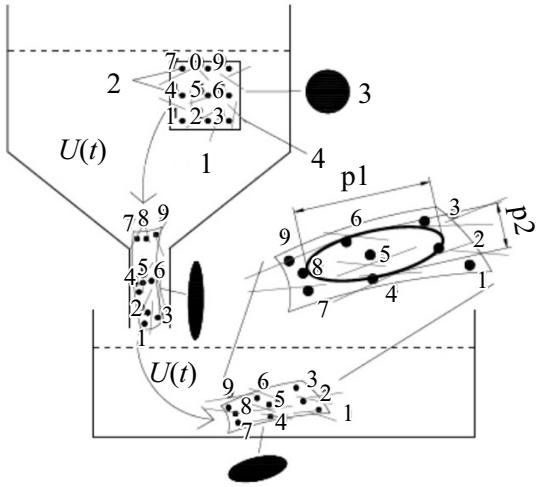

Fig. 1. Particle tracking scheme and ellipsoids of fiber orientation probability: 1 — particle tracking, 2 — particles, 3 — probability ellipsoid, and 4 — fibers.

where U is the velocity field, ρ is density, t is time, g is the acceleration of gravity, p is pressure, F_s is the surface tension force acting on free surfaces, γ is the fraction of fluid (mortar) in the cell, and U_r is the velocity field necessary to compress the interface between the mortar and air.

The density at any point in the computation domain was calculated as the weighted average of the volume fraction:

$$\rho = \gamma\rho_c + (1-\gamma)\rho_a ,$$

where ρ_c is the density of mortar and ρ_a is the density of air. When $\gamma = 1$, the cell is filled with mortar, and at $\gamma = 0$, it is filled with air.

A non-Newtonian incompressible Bingham-type fluid model was used [8]. This model describes the relationship between the strain rate and stress. The model is defined by the yield stress and the plastic viscosity.

The fiber orientation was analyzed by tracking particles in the mortar flow (see Fig. 1). The particle tracking was performed in the CFD postprocessing phase. The geometrical representation of particle tracking is shown in Fig. 1. The motion of a particle at a time step from t to $t+\Delta t$ was calculated using the velocity field $U(t)$:

$$x_i^{t+\Delta t} = x_i^t + U(t)\Delta t ,$$

where x_i^t are center coordinate of an ith particle at a time t, $x_i^{t+\Delta t}$ are its coordinates at the time $t+\Delta t$, and Δt is the time step.

It was assumed that the fiber orientation was mainly affected by the deformation gradient F^t, which partially has been proved by experimental measurements [7]. The deformation gradient was calculated using a set of particles around the central particle:

$$F_i^t = \frac{\partial x_i^t}{\partial x_i^0} \approx \frac{1}{N}\sum_{k=1}^{N}\begin{bmatrix} \frac{d_{i,k,x}^{T_{fin}}}{d_{i,k,x}^0} & \frac{\Delta d_{i,k,x}^{T_{fin}}}{d_{i,k,y}^0} & \frac{\Delta d_{i,k,x}^{T_{fin}}}{d_{i,k,z}^0} \\ \frac{\Delta d_{i,k,y}^{T_{fin}}}{d_{i,k,x}^0} & \frac{d_{i,k,y}^{T_{fin}}}{d_{i,k,y}^0} & \frac{\Delta d_{i,k,y}^{T_{fin}}}{d_{i,k,z}^0} \\ \frac{\Delta d_{i,k,z}^{T_{fin}}}{d_{i,k,x}^0} & \frac{\Delta d_{i,k,z}^{T_{fin}}}{d_{i,k,y}^0} & \frac{d_{i,k,z}^{T_{fin}}}{d_{i,k,z}^0} \end{bmatrix},$$

where N is the number of particles in the surrounding, $d_{i,k}^{t}$ is the distance between an *i*th central particle and a *k*th surrounding particle at time t, $\Delta d_{i,k,a}^{T_{fin}} = d_{i,k,a}^{T_{fin}} - d_{i,k,a}^{0}$, $(a = x, y, z)$. In order to reduce the computation time without a significant reduction in accuracy, only the diagonal terms of the deformation gradient were used to estimate the distribution of fiber orientation probability. In some cases, when the shear flow dominates, the off-diagonal members should also be considered. The length of a radius of the orientation ellipsoid is equal to the scaled diagonal term of deformation gradient and represents the probability of a fiber to be oriented in the direction of this radius.

In the case of multiple casting points, the mortar flow is separated. Then, there can be situations where some neighboring points move in another direction than the central point. This problem was solved by placing an additional restriction on the maximum distance through which a neighbor point can be moved away from the central one. If this distance was exceeded, the with a high probability, the flow could split, and this point was excluded from further calculations of the deformation gradient.

The diagonal terms of deformation gradient (F_{diag}^{t}) were used as the lengths of central axes of the ellipsoid of fiber orientation probability. A random fiber generator used the diagonal terms F_{diag}^{t} to calculate fiber orientation, which is defined by fiber projections on three orthogonal axes:

$$v_f^* = (\Delta x^*; \Delta y^*; \Delta z^*) = \left\{ \overline{\overline{U\left(-F_{i,11}^{t} + F_{i,11}^{t}\right)}}; \overline{\overline{U\left(-F_{i,22}^{t} + F_{i,22}^{t}\right)}}; \overline{\overline{U\left(-F_{i,33}^{t} + F_{i,33}^{t}\right)}} \right\},$$

$$v_f = v_f^* \cdot L_f \Big/ \left| v_f^* \right|,$$

where v_f^* is the fiber orientation vector, v_f is the fiber orientation vector whose length is equal to the fiber length L_f, $\overline{\overline{U(a,b)}}$ is a random number from the interval $[a,b]$, which is generated using a uniform random number generator, and Δx^*, Δy^*, and Δz^* are projections of the fiber orientation vector on coordinate axes.

2.2. Modeling of an impact

The displacement of the discrete lattice model was obtained using the explicit central difference scheme for integration with respect to time [19, 33]:

$$u^{t+\Delta t/2} = u^{t} + \left(\dot{u}^{t-\Delta t/2} + \frac{\Sigma F^{t}}{m_p} \Delta t \right) \Delta t \,.$$

The fiber-reinforced concrete was represented as a nonlinear discrete lattice model where nonlinearity of the material was taken into account. Each lattice member has a 1D constitutive equation, which makes the model simple, with few parameters and high computational efficiency. The cross-sectional areas of discrete lattice members were calculated using a homogenization technique where the energy equivalence criterion is used [5, 6, 18].

The nonlinear material behavior was related to the degradation of Young's modulus when cracks were growing [5, 18, 34]. A single damage variable was used:

$$E = E_{\text{init}} (1 - D),$$

where E_{init} is the initial Young's modulus, and D is a damage variable (equal to 0 for the undamaged material and 1 for the damaged one).

According to the recommendation for stress–strain curves given in [18, 35], the evolution of the damage variable was computed by the equation

$$D_{\text{tens}} = 1 - \frac{f_{\text{tens}}(\theta)\mu(\theta)\dfrac{1}{\varepsilon_{\text{tens}}(\theta)}}{E_{\text{init}}\left[\mu(\theta) - 1 + \left(\dfrac{\varepsilon}{\varepsilon_{\text{tens}}(\theta)}\right)\right]}, \tag{1}$$

where θ is the angle between the lattice member and the average fiber orientation, $f_{\text{tens}}(\theta)$ is the strength of fiber-reinforced concrete, $\mu(\theta)$ is the shape parameter of the stress-strain curve, $\varepsilon_{\text{tens}}(\theta) = \dfrac{f_{\text{tens}}}{E_{\text{init}}} k_{\varepsilon}(\theta)$ is the strains at the peak stress, and $k_{\varepsilon}(\theta)$ is a strain multiplier.

The damage variable in compression was calculated by an equation similar to Eq. (1) and was used at the next time step. The interaction between compression and tension damage variables was not taken into account, because not enough experimental data were available. However, the framework of continuum damage mechanics proposed can be slightly modified to take into account this interaction effect.

Material parameters were interpolated depending on the angle θ:

$$f_{\text{tens}}(\theta) = \left[f_{\text{tens,90}} + \cos(\theta)^n (f_{\text{tens,0}} - f_{\text{tens,90}}) \right] f(f_N) DIF_{\text{tens}}, \tag{2}$$

$$f_{\text{comp}}(\theta) = \left[f_{\text{comp,90}} + \cos(\theta)^n (f_{\text{comp,0}} - f_{\text{comp,90}}) \right] DIF_{\text{comp}}, \tag{3}$$

$$\mu(\theta) = \left[\mu_0 + \cos(\theta)^n (\mu_{90} - \mu_0) \right], \tag{4}$$

$$\cos\theta = \frac{\left| n_x F^t_{*,11} \right| + \left| n_y F^t_{*,22} \right| + \left| n_z F^t_{*,33} \right|}{\|n\| \cdot \left\| F^t_{\text{diag}} \right\|},$$

$$DIF_{\text{tens}} = \left(\dot{\varepsilon} / \dot{\varepsilon}_{st} \right)^{0.0013 \left[\log(\varepsilon/\varepsilon_{st}) \right]^{1.93}}$$

$$DIF_{\text{comp}} = \begin{cases} \left(\dot{\varepsilon} / \dot{\varepsilon}_{sc} \right)^{0.0055 \left[\log(\varepsilon/\varepsilon_{st}) \right]^{1.951}} & \text{for } \dot{\varepsilon} \geq \dot{\varepsilon}_{sc} \\ 0 \qquad \text{for } \dot{\varepsilon} < \dot{\varepsilon}_{sc} \end{cases},$$

where $f_{\text{tens,90}}$ and $f_{\text{comp,90}}$ are the tensile and compressive strengths perpendicularly to the fiber orientation, and $f_{\text{tens,0}}$ and $f_{\text{comp,0}}$ are the tensile and compressive strengths along the fiber orientation; n is a parameter characterizing the accuracy of fiber alignment; f_N is the average number of the fibers crossing a particular cross section; $f(f_N)$ is the ratio between the number of the fibers crossing a particular cross section in the oriented-fiber concrete and in the current case; DIF_{tens} and DIF_{comp} are dynamic increase factors; $n = (n_x, n_y, n_z)$ is the orientation vector of lattice member; F^t_{*ii} is the diagonal term of deformation gradient obtained by interpolation between the nearest points; $\dot{\varepsilon}$ is strain rate; $\dot{\varepsilon}_{sc} = 1.2 \cdot 10^{-5}$ 1/s and $\dot{\varepsilon}_{st} = 1.0 \cdot 10^{-6}$ 1/s. In this work, it was found that $n = 2$ for the cases analyzed [1].

2.3. Overall algorithm

The numerical modeling framework of a self-compacting high-performance fiber-reinforced concrete consisted of three main steps. At the first step, the two-phase incompressible fluid flow problem was solved. The velocity field $U(t)$, fluid volume fraction $\gamma(t)$, and pressure fields were found. At the second step, the CFD postprocessing was performed. It consisted of the particle tracking algorithm and calculation of the fiber orientation ellipsoid at each point. This ellipsoid was determined when particles were located in their final position and the flow velocity was zero and was used to generate a random fiber network to calculate the fiber orientation coefficient η_θ and the number of fibers per unit area F_n [36]:

$$\eta_\theta = \int_{\theta_{\min}}^{\theta_{\max}} p(\theta) \cos^2\theta \, d\theta, \tag{5}$$

$$F_n = n_f / A, \tag{6}$$

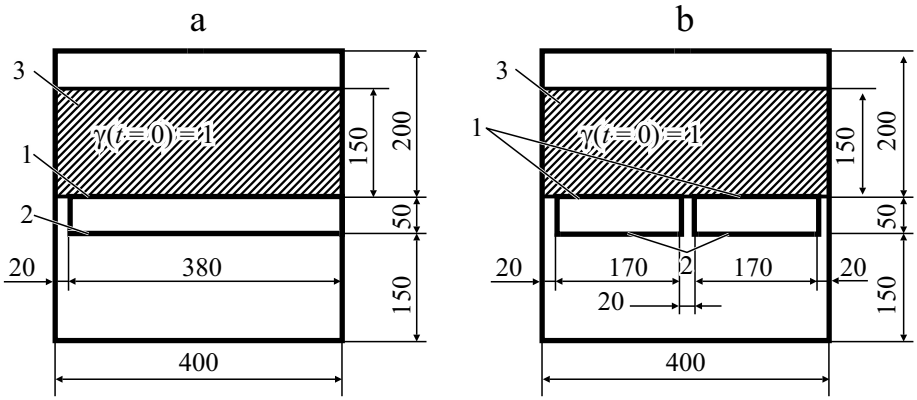

Fig. 2. Schematic of the CFD calculation model for one and three pouring points. Dimensions in mm: 1 — walls, 2 — atmospheric boundary, and 3 — initial conditions.

where $p(\theta)$ is the probability distribution function, $\cos\theta$ is cosine between the fiber axis and the neutral axis of the beam; n_f is the average number of the fibers crossing the cross section of interest; $\theta_{\min}$ and $\theta_{\max}$ are the minimum and maximum values of fiber orientation angle; and A is area of the cross section.

At the third step, the impact modeling was performed. It was assumed that the fiber orientation did not change in the curing process. The discrete lattice model was created using a tetrahedron mesh generation routine. Into each edge of the tetrahedron, a lattice member was inserted. The impact was modeled using an explicit time integration algorithm. As a result, the load bearing capacity, which included the peak load and energy absorption measures, was estimated.

3. Results

The influence of casting technology on the impact properties of the fiber-reinforced concrete were studied by the numerical methods proposed. Two different casting technologies were considered. The first one, denoted as 1P, used a single pouring point, and the second one, denoted as 3P, used three pouring points. The first technology provided a better fiber orientation, but it took more casting time.

The mortar was made from a type-1 Portland cement and silica fume. Silica sand with a grain size less than 0.5 mm was included as a fine aggregate, and silica flour (with 2-μm grains) was used as a filler. Straight steel fibers of length 13 mm and diameter 0.2 mm, with a tensile strength of 2500 MPa, were added to the mortar in amount of 2 vol.%. In order to obtain an adequate flowability and viscosity sufficient to prevent fiber segregation, a high-performance water-reducing agent, polycarboxylate superplasticizer with a density of 1.06 g/cm^3, to the extent of 2 wt.% of cement, was also included.

A special mixing sequence was adopted. First, all of the dry materials were premixed for approximately 10 min to achieve a good dispersion. Next, water mixed with the superplasticizer was added to the dry materials and mixed for additional 10 min. When the mixture obtained a sufficient fluidity, fibers were carefully dispersed and mixed for 5 min. More details on the materials and their preparation technology can be found in [36]. The mixing process was not modeled numerically, assuming that the fiber orientation after mixing was isotropic.

3.1. Analysis of fiber orientation

A schematic of the CFD model is shown in Fig. 2. On its walls, the zero gradient boundary condition of γ, no-slip condition of velocity U, and zero pressure flux condition were prescribed. The atmospheric boundary conditions were approximated using the zero velocity condition, zero total pressure, and zero value of γ. The initial location of γ is shown in

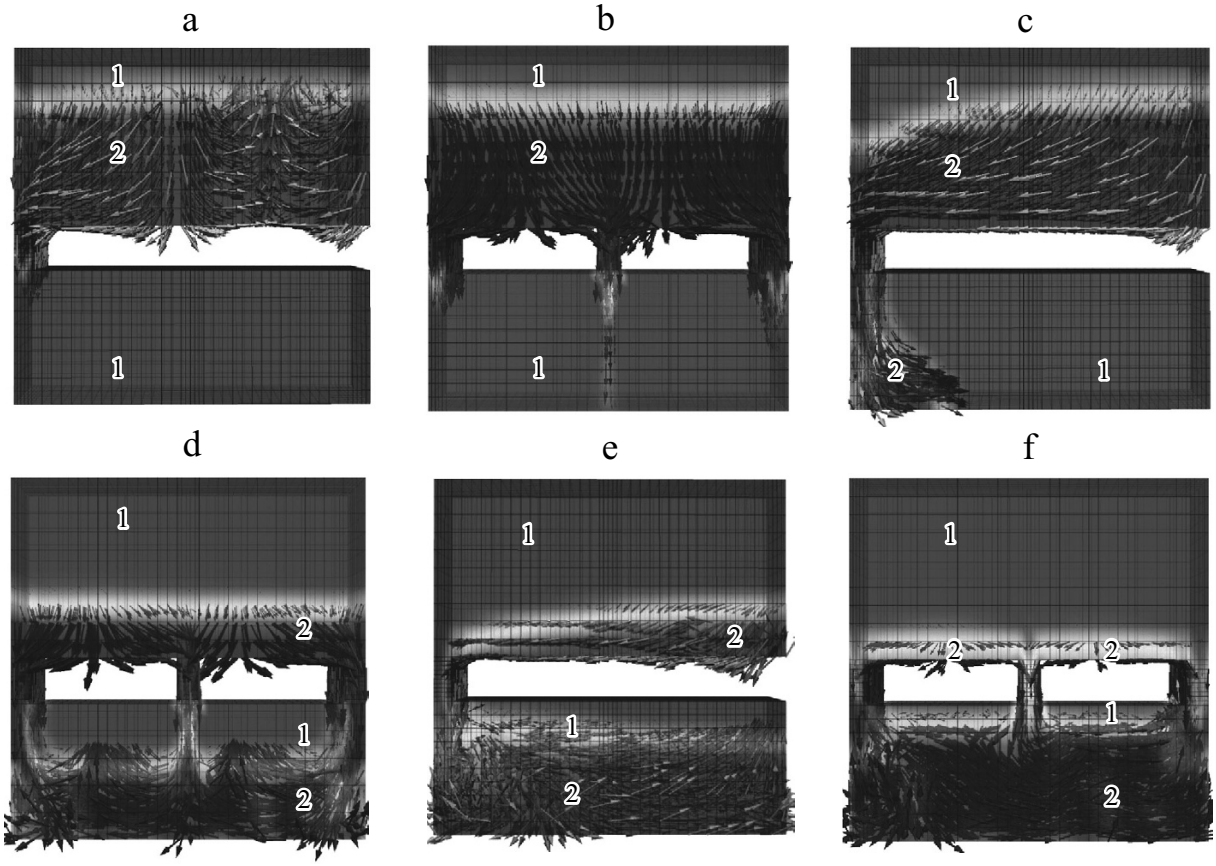

Fig. 3. Concrete flow in the case of single (a, c, e) and three pouring points (b, d, f) in 1 (a, b) and 10 s (c, d) and at the final time (e, f): filled with air (1) and mortar (γ =1) (2).

Fig. 2 as a hatched area. In the case of a single pouring point, opening dimensions were 20 × 100 mm, which could provide a flow speed of about 3l/min. In the case of three pouring points, the opening had the same dimensions. All three openings were opened and closed at the same time.

In the present study, the yield stress of the self-compacting high-strength fiber-reinforced concrete was 100 Pa and its plastic viscosity was 50 Pa · s [8]. Air was described as a Newtonian material with a kinematic viscosity of $1.48 \cdot 10^{-5}$ N/s. The surface tension forces were computed using a surface tension coefficient $s = 0.07$ N/m and curvature of the interface [32].

The velocity field and γ of mortar flow are shown in Fig. 3. The arrows indicate the principal directions of velocity. It can be seen that, after 10 s, the 3P sample was filled more than 1P. However, the velocity field was more nonuniform for the 3P sample. The velocity gradient and wall effects in 1P samples aligned fibers more closely to the neutral axis of the beam.

In the case of 1P technology, the bottom layer of sample had a relatively good fiber orientation, — most of the orientation ellipsoids were stretched in the direction of beam axis. In the opposite side of pouring point, fibers were inclined at angles from 0 to 45° to the beam axis. This effect has also been observed experimentally [7]. In the 3P technology, ellipsoids were stretched only partly in the direction of beam axis, and their average orientation was not so good as in the 1P case.

The CFD postprocessing results of fiber orientation were compared with experimental measurements. It is a common approach to measuring fiber orientations in a particular cross section using the image analysis method [36]. In three-point bending, this cross section is in the middle of beam, where the tensile stress is maximum. A random fiber generator was used to produce fibers in the middle part (of dimensions 100 × 100 × 50 mm) of the beam (see Fig. 4). The number of the fibers crossing the middle cross section and their orientation angles were calculated using a virtually generated structure. As a result, the fiber orientation factor (see Eq. (5)) and the number of the fibers crossing a unit area (see Eq. (6)) were found. Since random

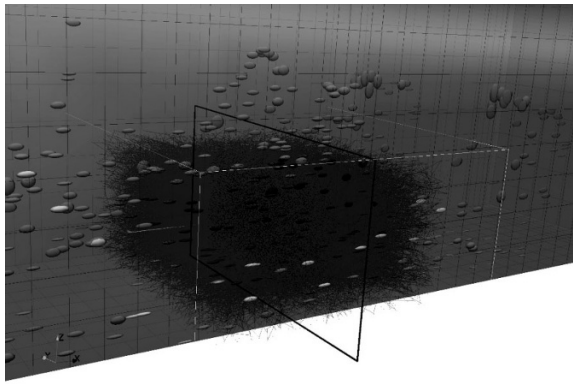

Fig. 4. Random fiber network for an analysis of the middle cross section.

TABLE 1. Comparison of Fiber Orientation Parameters Obtained Experimentally and by Simulation

Sample	Parameter	Experiment	Simulation	Difference, %
1P	η_θ	0.66	0.69±0.004	4.54
	F_n, fibers/cm^2	47.02	45.03±1.17	–4.42
3P	η_θ	0.64	0.65±0.003	1.56
	F_n, fibers/cm^2	36.76	40.97±0.96	11.45

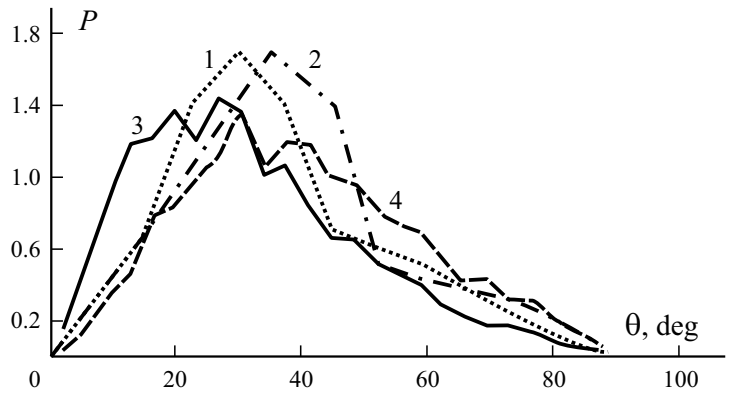

Fig. 5. Distribution of probability P of the fiber orientation angle θ: 1P — experiment (1) and simulation (3); 3P — experiment (2) and simulation (4).

fiber generation is a stochastic process, the average values and the standard deviation were calculated using five independent runs. The numerically estimated and experimentally measured results for the middle cross section are shown in Table 1, and a rather good agreement with experimental results, is seen to axist.

The probability density function (PDF) of the fiber orientation angle θ in the middle cross section of the beam is shown in Fig. 5. As is seen, the average orientation angle in the 1P casting technology is smaller than in the 3P one, but the PDF function in the 1P technology is shifted to the left more than in the 3P one, indicating a better fiber orientation with respect to the neutral axis of the beam. The experimentally measured PDE functions are in good agreement with numerical results.

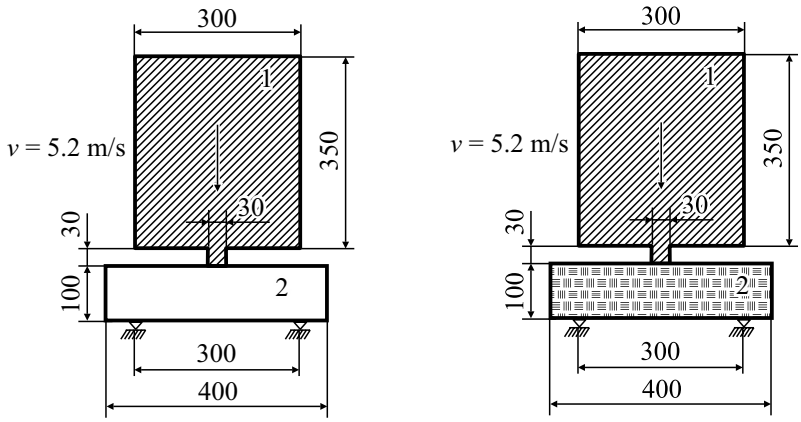

Fig. 6. Schematic and dimensions (mm) of the sample: 1 — steel and 2 — concrete.

TABLE 2. Material Parameters* in Impact Loading

Tension		Compression
In the fiber direction	Perpendicular to fibers	
$f_{tens,0} = 18$ MPa	$f_{tens,90} = 12$ MPa	$f_{comp} = 211$ MPa
$\mu_{tens,0} = 1.4$	$\mu_{tens,90} = 1.6$	$\mu_{comp} = 1.4$
$k_{\varepsilon,tens,0} = 5$	$k_{\varepsilon,tens,90} = 5$	$k_{\varepsilon,comp} = 1$
	$E = 46.7$ GPa	

*obtained by fitting the experimental results presented in [36, 37].

3.2. Impact modeling in three-point bending

The impact response of a 100 × 100 × 400 mm beam in three-point bending was tested virtually and compared with experimental results. Details on the numerically tested specimen are shown in Fig. 6. The impact force was applied by a steel weight of dimensions 350 × 300 × 100 mm, whose speed was 5.2 m/s at the instant of contact with the beam. The contact area was 100 × 30 mm. The average density of concrete was 2500 kg/m^2 and of steel 7800 kg/m^2.

The values of material parameters are shown in Table 2. It was assumed, and has also been prooved by experiments [37], that the compressive strength is not significantly affected by fiber orientation [37]. The average compressive strength was 210 MPa. However, fiber orientation had a significant effect on the tensile properties. In the case where the average fiber orientation was perpendicular to the neutral axis of the beam, the tensile strength was 12 MPa, but it reached 18 Pa when the orientation was parallel to the neutral axis. At other fiber orientation angles, a the nonlinear interpolation according to Eqs. (2)-(4) was performed.

The potential damage zones were described by using the damage variable D. In Fig. 7, the potential cracked (damaged) zones found numerically and observed experimentally in three-point bending are shown. In the numerical model, the spheres show the damaged zones with $D > 0.99$. It can be seen that, in the numerical model, the main crack has developed in the central cross section of the beam, which agrees with experimental observations (see Fig. 7). However, a shear crack, starting from the support and propagating to the impact point, can also appear, which has been observed in some experimental specimens [37].

Similar deformed schemes of samples made by using the 1P and 3P technologies were obtained. As is seen, the most part of displacements had developed due to the damaged area in the central cross section of the beam. A similar deformed scheme has also been observed experimentally [36, 37].

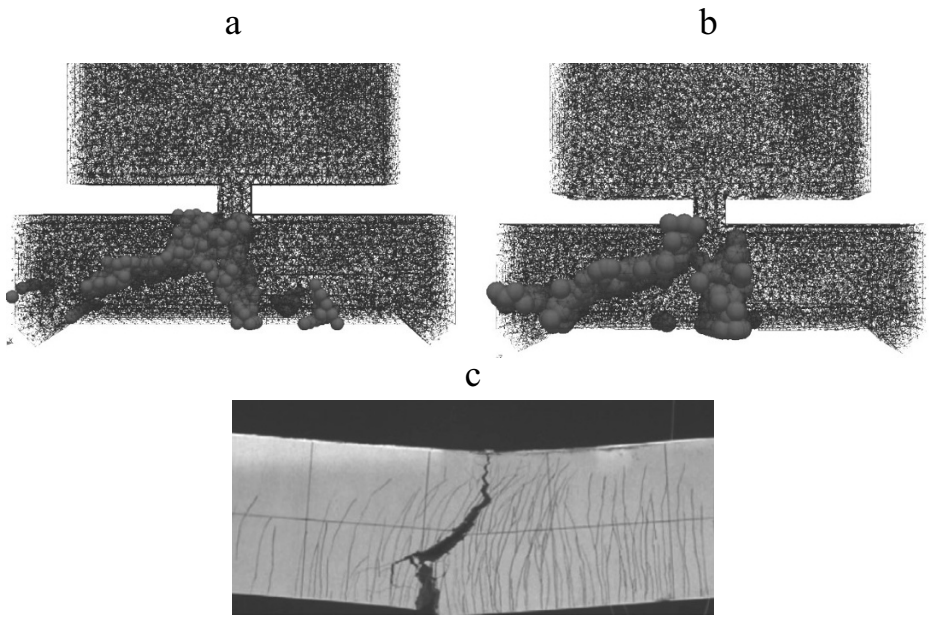

Fig. 7. Potential location of cracks according to simulation results for 1P (a) and 3P (b) casting and experimental observations [37]. Explanation in the text.

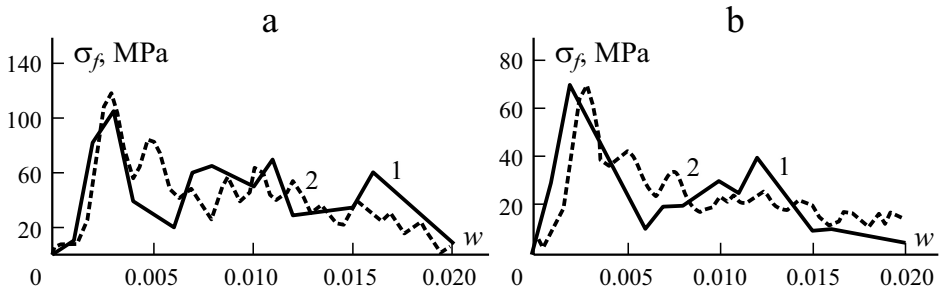

Fig. 8. Experimental (1) and simulated (2) flexural stress σ_f –normalized deflection w curves of samples 1P (a) and 3P (b).

Relationships between the flexural stress and the normalized deflection (the ratio between the deflection and beam span) are shown in Fig. 8. The peak flexural stress for the beam made by the 1P technology was about 105 MPa and about 70 MPa for the 3P sample. The numerical models were able to estimate the peak load with a good agreement (difference less than 5%) with experiments. We should also mention that the energy absorbed by the 1P samples was by 35% higher than that absorbed by the 3P ones.

4. Conclusions

A numerical framework modeling technique for the casting process and virtual testing of the structure of an impact-loaded self-compacting high-performance fiber-reinforced concrete is proposed. A two-phase flow of mortar is modeled as an incompressible continuum fluid model, where the velocity field is used to estimate the local fiber orientation employing the deformation gradient. A nonlinear strain rate- and local-fiber-orientation-dependent constitutive law for the discrete lattice model is also proposed. The numerically modeled single-point pouring technique was found to provide a beam with

a better fiber orientation and better impact properties then the three-point pouring one. Similar results for the local fiber orientation in the central cross section of the beam and the impact strength and energy absorbing properties have also been observed in experiments.

Further investigations and optimization of the casting technology a needed for more complex structures.

Acknowledgements. The financial support of European Regional Development Fund project Nr.1.1.1.1/16/A/007 "A New Concept for Sustainable and Nearly Zero-Energy Buildings" is gratefully acknowledged.

REFERENCES

1. A. Abrishambaf, V. M. C. F. Cunha, and J. A. O. Barros, "A two-phase material approach to model steel fibre reinforced self-compacting concrete in panels," Eng. Fract. Mech., **162,** 1-20 (2016). doi:10.1016/j.engfracmech.2016.04.043.
2. E. V. Sarmiento, M. A. N. Hendriks, M. R. Geiker, and T. Kanstad, "Modeling the influence of the fibre structure on the structural behaviour of flowable fibre-reinforced concrete," Eng. Struct., **124,** 186-195 (2016). doi:10.1016/j.engstruct.2016.05.053
3. V. M. C. F. Cunha, J. A. O. Barros, and J. M. Sena-Cruz, "An integrated approach for modeling the tensile behaviour of steel fibre reinforced self-compacting concrete," Cem. Concr. Res., **41**, 64-76 (2011). doi:10.1016/j.cemconres.2010.09.00
4. M. Roy, C. Hollmann, and K. Wille, "Influence of volume fraction and orientation of fibers on the pullout behavior of reinforcement bar embedded in ultra high performance concrete," Constr. Build. Mater., **146**, 582-593 (2017). doi:10.1016/j.conbuildmat.2017.04.08
5. J. Sliseris, H. Andrä M. Kabel, B. Dix, B. Plinke, O. Wirjadi, et al., "Numerical prediction of the stiffness and strength of medium density fiberboards," Mech. Mater., **79**, 73-84 (2014). doi:10.1016/j.mechmat.2014.08.005.
6. J. Sliseris, H. Andrä, M. Kabel, B. Dix, and B. Plinke, "Virtual characterization of MDF fiber network," Eur. J. Wood Wood Prod., **75**, 397-407 (2017). doi:10.1007/s00107-016-1075-5.
7. B. Zhou and Y. Uchida, "Influence of flowability, casting time and formwork geometry on fiber orientation and mechanical properties of UHPFRC," Cem. Concr. Res., **95**, 164-177 (2017). doi:10.1016/j.cemconres.2017.02.017.
8. R. Deeb, B. L. Karihaloo, and S. Kulasegaram, "Reorientation of short steel fibres during the flow of self-compacting concrete mix and determination of the fibre orientation factor," Cem. Concr. Res., **56**, 112-120 (2014). doi:10.1016/j.cemconres.2013.10.002.
9. F. Kolařík, B. Patzák, and L. N. Thrane, "Modeling of fiber orientation in viscous fluid flow with application to self-compacting concrete," Comput. Struct., **154**, 91-100 (2015). doi:10.1016/j.compstruc.2015.03.007
10. W. Ren, Z. Yang, R. Sharma, C. Zhang, and P. J. Withers, "Two-dimensional X-ray CT image based meso-scale fracture modeling of concrete," Eng. Fract. Mech., **133**, 24-39 (2015). doi:10.1016/j.engfracmech.2014.10.016
11. A. Qsymah, R. Sharma, Z. Yang, L. Margetts, and P. Mummery, "Micro X-ray computed tomography image- based two-scale homogenisation of ultra high performance," Fibre Reinf. Concrete, **130**, 230-240 (2016).
12. Y. Su, C. Wu, J. Li, Z.-X. Li,and W. Li, "Development of novel ultra-high performance concrete: From material to structure," Constr. Build. Mater., **135**, 517-528 (2017). doi:10.1016/j.conbuildmat.2016.12.175.
13. M. Singh, A. H. Sheikh, M. S. Mohamed Ali, P. Visintin, and M. C. Griffith, "Experimental and numerical study of the flexural behaviour of ultra-high performance fibre reinforced concrete beams," Constr. Build. Mater., **138**, 12-25 (2017). doi:10.1016/j.conbuildmat.2017.02.002.
14. M. Bruggi, "Generating strut-and-tie patterns for reinforced concrete structures using topology optimization," Comput. Struc., **87**, 1483-1495 (2009). doi:10.1016/j.compstruc.2009.06.003
15. B. Sun, X. Wang, and Z. Li,. "Meso-scale image-based modeling of reinforced concrete and adaptive multi-scale analyses on damage evolution in concrete structures," Comput. Mater. Sci., **110**, 39-53 (2015). doi:10.1016/j.commatsci.2015.07.050.
16. G. F. Zhao, "Developing a four-dimensional lattice spring model for mechanical responses of solids," Comput. Methods Appl. Mech. Eng., **315**, 881-895 (2017). doi:10.1016/j.cma.2016.11.034

17. J. Šliseris, L. Gaile, and L. Pakrastiņš, "Deformation process numerical analysis of T-stub flanges with pre-loaded bolts," Procedia Eng., 172, (2017). doi:10.1016/j.proeng.2017.02.173.
18. J. Sliseris, "Numerical analysis of reinforced concrete structures with oriented steel fibers and re-bars," Eng. Fract. Mech., **194**, 337-349 (2018). doi:10.1016/j.engfracmech.2018.03.017.
19. N. H. T. Nguyen, H. H. Bui, G. D. Nguyen, J. Kodikara, S. Arooran, and P. Jitsangiam, "A thermodynamics-based cohesive model for discrete element modeling of fracture in cemented materials," Int. J. Solids Struct., **117**, 159-176 (2017). doi:10.1016/j.ijsolstr.2017.03.027
20. C. Jiang, G. F. Zhao, and N. Khalili, "On crack propagation in brittle material using the distinct lattice spring model," Int. J. Solids Struct., **118-119**, 1339-1351 (2017). doi:10.1016/j.ijsolstr.2017.04.024
21. A. Yaghoobi and M. G. Chorzepa, "Fracture analysis of fiber reinforced concrete structures in the micropolar peridynamic analysis framework," Eng. Fract. Mech., **169**, 1-13 (2016). doi:10.1016/j.engfracmech.2016.11.004
22. J. Smith, G. Cusatis, D. Pelessone, E. Landis, J. O'Daniel, and J. Baylot, "Discrete modeling of ultra-high-performance concrete with application to projectile penetration," Int. J. Impact Eng., 65, 13-32 (2014). doi:10.1016/j.ijimpeng.2013.10.008
23. N. Banichcuk, "Optimization problems for elastic anisotropic bodies," Arch. Mech., **3**, 347-363 (1981).
24. P. Pedersen, "On optimal orientation of orthotropic materials," Struct. Optim., **1**, 101-106 (1989).
25. J. Lellep and J. Majak, "Nonlinear constitutive behavior of orthotropic materials," Mech. Compos. Mater., **36**, No. 4, 261-264 (2000).
26. J. Lellep and J. Majak, "On optimal orientation of nonlinear elastic orthotropic materials," Struct. Optim., **14**, 116-120 (1997).
27. M. Rovati and A. Taliercio, "Stationarity of the strain energy density for some classes of anisotropic solids," **40**, 6043-6075 (2003). doi:10.1016/S0020-7683(03)00371-8
28. J. Majak and M. Pohlak, "Optimal material orientation of linear and non-linear elastic 3D anisotropic materials," Meccanica, **45**, 671-680 (2010).
29. J. Majak and M. Pohlak, "Decomposition method for solving optimal material orientation problems," Compos. Struct., **92**, 1839-1845 (2010). doi:10.1016/j.compstruct.2010.01.015.
30. D. Jeong and J. Kim, "Conservative Allen–Cahn–Navier–Stokes system for incompressible two-phase fluid flows," Comput. Fluids, **156**, 239-246 (2017). doi:10.1016/j.compfluid.2017.07.009
31. Z. Z. Hu, D. Greaves, and A. Raby, "Numerical wave tank study of extreme waves and wave-structure interaction using OpenFoam®," "Ocean Eng., **126**, 329-342 (2016). doi:10.1016/j.oceaneng.2016.09.017
32. L. F. Chen, J. Zang, A. J. Hillis, G. C. J. Morgan, and A. R Plummer, "Numerical investigation of wave–structure interaction using OpenFOAM," Ocean Eng., **88**, 91-109 (2014). doi:10.1016/j.oceaneng.2014.06.003
33. J. Šliseris, L. Gaile, and L. Pakrastiņš, "Numerical analysis of behaviour of cross laminated timber (CLT) in blast loading," IOP Conf. Ser. Mater. Sci. Eng., vol. 251 (2017). doi:10.1088/1757-899X/251/1/012105
34. J. Sliseris, L. Yan, and B. Kasal, "Numerical modeling of flax short fibre reinforced and flax fibre fabric reinforced polymer composites," Composites: Part B., **89**, 143-154 (2016). doi:10.1016/j.compositesb.2015.11.038
35. A. K. Someh and N. Saeki, "Prediction for the stress-strain curve of steel fiber reinforced concrete," Trans. Japan Concr. Inst., **18**, 175-182 (1996).
36. D. Y. Yoo, N, Banthia, S. T. Kang, and Y. S. Yoon, "Effect of fiber orientation on the rate-dependent flexural behavior of ultra-high-performance fiber-reinforced concrete," Compos. Struct., **157**, 62-70 (2016). doi:10.1016/j.compstruct.2016.08.02
37. D. Y. Yoo, N. Banthia, S. W. Kim, and Y. S.Yoon, "Response of ultra-high-performance fiber-reinforced concrete beams with continuous steel reinforcement subjected to low-velocity impact loading," Compos. Struct., **126**, 233–245 (2015). doi:10.1016/j.compstruct.2015.02.058